https://doi.org/10.1016/j.addma.2023.103934

Fabrication of predesigned 3D carbon based microstructures via two-photon vat photopolymerization and susceptor-assisted microwave post-processing

Ka-Wai Yeung[a], Zhenjia Huang[a], Chi-Yeung Mang[a], Chak-Yin Tang[a]*, Wing-Cheung Law[a], Gary Chi-Pong Tsui[a], Xin Zhao[b]

[a]Department of Industrial and Systems Engineering, The Hong Kong Polytechnic University, Hong Kong, China

[b]Department of Applied Biology and Chemical Technology, The Hong Kong Polytechnic University, Hong Kong, China

*Corresponding author

Email address: cy.tang@polyu.edu.hk, Phone: +852 2766 6608, Fax: +852 2362 5267

Postal address: Department of Industrial and Systems Engineering, The Hong Kong Polytechnic University, Hung Hom, Kowloon, Hong Kong, China.

CRediT author statement

Ka-Wai Yeung: Conceptualization, Methodology, Investigation, Writing - Original Draft, Data Curation, Visualization; **Zhenjia Huang:** Investigation, Data Curation **Chi-Yeung Mang:** Data Curation; **Chak-Yin Tang*:** Conceptualization, Supervision, Writing - Review & Editing, Funding acquisition; **Wing-Cheung Law:** Writing - Review & Editing; **Gary Chi-Pong Tsui:** Writing - Review & Editing; **Xin Zhao:** Writing - Review & Editing.

Fabrication of predesigned 3D carbon based microstructures via two-photon vat photopolymerization and susceptor-assisted microwave post-processing

Ka-Wai Yeung[a], Zhenjia Huang[a], Chi-Yeung Mang[a], Chak-Yin Tang[a]*, Wing-Cheung Law[a], Gary Chi-Pong Tsui[a], Xin Zhao[b]

[a]Department of Industrial and Systems Engineering, The Hong Kong Polytechnic University, Hong Kong, China

[b]Department of Applied Biology and Chemical Technology, The Hong Kong Polytechnic University, Hong Kong, China

*Corresponding author

Email address: cy.tang@polyu.edu.hk, Phone: +852 2766 6608, Fax: +852 2362 5267

Postal address: Department of Industrial and Systems Engineering, The Hong Kong Polytechnic University, Hung Hom, Kowloon, Hong Kong, China.

Fabrication of predesigned 3D carbon based microstructures via two-photon vat photopolymerization and susceptor-assisted microwave post-processing

Abstract

This study presents a fabrication strategy for 3D carbon microstructures using via two-photon vat photopolymerization (2p-VPP) and susceptor-assisted microwave pyrolysis (SMWP). Fabricating carbon-based electrode materials with miniaturized functional structures is pivotal for developing high-performance electrochemical microdevices. However, efficiently producing these structures in the submicron regime with desired materials is still challenging. To address this, a hybrid microfabrication strategy was developed, and 3D carbon-based microstructures with submicron resolution were successfully produced. A carbon nanotube nanocomposite photoresist (SCNT-PR1) with improved dispersibility was first prepared. After a comprehensive printability assessment, 3D microstructures with a resolution of 833 ± 54 nm were produced using 2p-VPP. Through SMWP, the microstructures were transformed into pyrolytic carbon (PyC) nanocomposite microstructures with retained geometrical features. SMWP was shown to produce PyC with a less disordered carbon atomic structure, thanks to the accelerated pyrolysis reaction under MW irradiation, when compared to pyrolysis using a conventional furnace. The resistivity was reduced by over 75% from 0.69 ± 0.13 Ω cm to 0.16 ± 0.01 Ω cm, and enhanced electrochemical performance was confirmed. The fabricated PyC nanocomposite showed a further 12% reduction in electrical resistivity and a 20% lower charge transfer resistance for the redox reaction when using SCNT-PR1 as the precursor. Overall, this hybrid fabrication strategy demonstrates the advantages of producing 3D carbon microstructures with precise control over the geometric features and enhancing electrical and electrochemical properties compared to the conventional

pyrolysis method. Its potential could be extended to the fabrication of miniaturized electrochemical devices, including microelectronics and point-of-care devices.

Keywords: hybrid microfabrication; pyrolysis; carbon nanomaterial; pyrolytic carbon metamaterial; microwave

1 Introduction

Carbon-based materials have found numerous practical applications, including energy conversion devices [1], chemical analysis [2], point-of-care devices [3], and health monitoring systems [4]. The ever-increasing demands for high-performance energy storage or sensing microdevices have led to the development of advanced electrode materials with 3D functional microstructures that can reduce the footprint area without compromising the functional performance [5, 6]. Additive manufacturing (AM) technologies offer the possibility of fabricating predesigned complex 3D structures with a wide range of materials. However, it is technically challenging to produce 3D carbon-based structures with submicron features (<1 μm) [7], and for a competent fabrication strategy with high throughput, reduced time cost is certainly needed. Laser-based two-photon vat photopolymerization (2p-VPP) technology, also known as direct laser writing (DLW), leverages near-infrared pulsed femtosecond laser to enable the production of high-resolution microstructures. Unlike other micro-/nano-fabrication technologies such as nanoimprint [8], DLW offers true 3D printing capabilities, rendering this technology an emerging and powerful tool in various applications, including nanophotonics [9], bioscaffolds [10], and micro-actuators [11, 12]. Furthermore, DLW also enables the fabrication of advanced metamaterials that exhibit "smaller but stronger" phenomena, which facilitates the production of mechanically durable structures for a longer service life [13]. This is particularly crucial to the design of electrodes for electronics such as supercapacitor and batteries, where achieving precise control over both the structural geometry can be beneficial to enhance the performance and mechanical stability. However, conventional fabrication methods often struggle to effectively addressing these critical aspects, leading to a compromise between mechanical robustness and enhanced electrochemical properties [14]. Although DLW offers great potential for fabricating

microstructures with precise controlled geometry, only polymeric 3D structures can be produced, which restricts its application in fabricating advanced miniaturized electrochemical devices. Therefore, it is necessary to derive innovative strategies for fabricating structures with diverse material choices.

Various fabrication strategies have been developed to mitigate the material limitations of DLW technology. For instance, the templated-assisted approach utilizes DLW-printed structures as the templates, and varied materials can be deposited onto the structure [15, 16]. These hybridized techniques enable the generation of hollow metal or ceramic microstructures that retain the geometrical features of the template after the template's removal [17]. Other techniques, such as two-photon reduction of metal precursors, have also been reported [18], but are limited to 2.5D structures. Recent studies have also reported innovative strategies for producing 3D metallic and ceramic structures through post-thermal treatment [19-21]. Chemically engineered photoresists were developed by incorporating metal clusters, preceramic polymers, or ceramic nanoparticles. After pyrolysis at elevated temperatures, the organic constituents slowly degraded, and the metal or ceramic clusters were sintered while maintaining the predesigned geometry. These pioneering works have conquered the inherent constraint of DLW and paved a new way for fabricating structures with submicron resolutions, other than polymers, broadening the application of DLW technology. However, these approaches involve lengthy fabrication processes, and further development is still needed to expand the material class and, more importantly, seek a more effective and efficient fabrication strategy with high reproducibility.

Microwave (MW) technology has been used as a sustainable alternative for various thermal treatments, covering chemical synthesis [22, 23], metal [24], and ceramic sintering [25], due to the intrinsic heating mechanism involving fast and volumetric

heating and high energy penetration. Compared to other heating methods, such as conventional oven heating and infrared heating, which only provide superficial heating of materials, MW heating enables deeper energy penetration owing to its specific wavelength within the electromagnetic spectrum [26]. Furthermore, MW heating is not constrained by the thermal inertia of the furnace components or the thermal conductivity of the materials, thereby achieving higher heating rates even over larger heating volumes. This technology has been employed for waste management, such as biomass pyrolysis and carbon fiber recovery, to convert waste into value-added carbon products [27]. In addition, it was reported that MW irradiation could initiate the pyrolysis reaction with lower activation energy and a faster reaction rate. Therefore, it is conceivable that developing a microfabrication strategy that utilize DLW and MW technologies could pave the way for an efficient fabrication process for 3D carbon-based microstructure, enabling precise control over their architecture. Despite the said benefits, direct MW processing is material restricted, as its heating efficiency depends heavily on the dielectric and magnetic properties of the materials. The susceptor-assisted MW process, where MW absorbers aid the heating process, can overcome the processing difficulties for low-loss or MW transparent materials, offering a controllable, reliable, and reproducible process [25, 28]. However, there is still a lack of studies investigating the effectiveness of the susceptor-assisted MW process for the pyrolysis of 3D-printed synthetic polymers for electrochemical applications.

This study developed a hybrid strategy by leveraging the advantages of DLW and susceptor-assisted MW pyrolysis (SMWP) for generating predesigned 3D carbon microstructures, as illustrated in Figure 1. DLW offers precise generation of 3D structures with submicron resolution, while SMWP offers an efficient method for producing functional carbon structures with enhanced electrical and electrochemical performance

compared to conventional methods, due to the volumetric heating attributed to the combined mode of dielectric heating and conventional modes of heat transfer provided by the MW susceptor. The strategy offers an effective microfabrication technique with the potential to develop high-performance electrochemical microdevices with miniaturized functional structures made of carbon-based electrode materials. Carbon nanotube-containing nanocomposite photoresists (SCNTs-PR1) were prepared with improved dispersion as a model precursor for the 3D carbon microstructures. It was anticipated that CNTs can act as an MW absorber to aid the pyrolysis and reduce the overall shrinkage of the structure during SMWP, resulting in a PyC product with enhanced electrical and electrochemical properties compared to the one without nanofillers. Metamaterials were generated through DLW after a comprehensive printability assessment for suitable laser writing conditions. The 3D SCNTs-PR1 microstructures were successfully converted to 3D pyrolytic carbon (PyC) microstructures through SMWP, and the geometrical features were retained. Compared to conventional pyrolysis, SMWP can convert the polymer precursors to PyC products with a more ordered carbon atomic structure due to the accelerated pyrolysis reaction under MW irradiation. As a result, the PyC product showed enhanced electrical and electrochemical performance compared to the samples fabricated through conventional pyrolysis. The effects of SMWP conditions on the properties of the PyC product were studied and compared. On the whole, the presented hybrid strategy offers exciting potential for pushing forward the development of electrochemical microdevices, such as microelectronics and point-of-care devices.

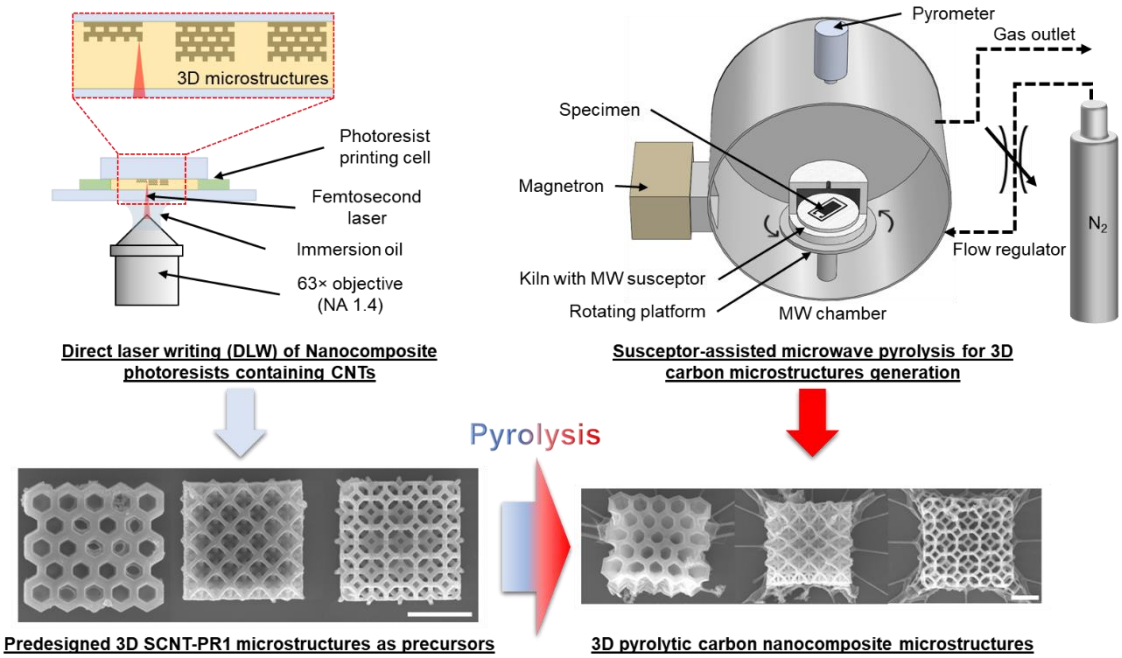

Figure 1 Illustration of the hybrid fabrication strategy for generating predesigned 3D carbon microstructures using DLW and SMWP

2 Experimentation

2.1 Preparation of MWCNTs nanocomposite photoresist

Multiwalled carbon nanotubes (MWCNT, purity > 95 wt.%, inner diameters of 3 - 5 nm, outer diameters of 8 - 15 nm, and tube lengths of ~50 μm) were purchased from Chengdu Organic Chemicals Co. Ltd., China. The MWCNTs were modified through a two-step functionalization to improve the dispersibility of the MWCNTs. First, MWCNTs were acid treated by refluxing in nitric acid and sulfuric acid (volume ratio of 1:3) at 80 °C for 12 h under vigorous stirring. The acid-treated MWCNTs (Ac-MWCNTs) were then washed with excessive distilled water until the residual became neutral, followed by vacuum drying at 80 °C overnight. Subsequently, thiol functionalization was adopted to improve the dispersibility of MWCNTs in the acrylate-based photoresist. The 5 mg of Ac-MWCNTs were redispersed in 5 mL of acetone under 5 min ultrasonication. Then, 0.5 g of Pentaerythritol tetrakis (3- mercaptopropionate) (PETMP, >95%, Sigma

Aldrich) was then dissolved into the dispersion under ultrasonication for 30 min. The mixture was stirred vigorously for an additional 12 h at room temperature. The thiol-functionalized MWCNTs (S-MWCNTs) were obtained through the covalent functionalization of PETMP on the Ac-MWCNTs surface [29]. The mixture was filtered, and the S-MWCNTs were collected by drying overnight at 60 °C in a vacuum oven. The characterizations of MWCNTs before and after chemical treatment are presented in Figure S1 in the Supplementary Information.

After the two-step functionalization, S-MWCNTs were added to 2 mL of acetone under ultrasonication in iced water for 30 min. Then, the IP-DIP photoresist (Nanoscribe GmbH, Germany) was dissolved in the S-MWCNTs acetone solution and vigorously stirred overnight. Subsequently, to enhance the photosensitivity of the MWCNNTs nanocomposite photoresist, 2 wt.% of photoinitiator, 2-Benzyl-2-(dimethylamino)-4'-morpholinobutyrophenone (BDMP, 97%, Sigma Aldrich) was also added. The mixture was ultrasonicated and vigorously stirred for 2 h, followed by vacuum drying at 30 °C for 12 h to completely remove the solvent. After drying, the photoresist was centrifuged at 6000 rpm for 30 min. Large agglomerate of CNTs were removed to ensure the homogeneity of the photoresist, which may also lower the actual CNT percentage in the photoresist. The residual content after the decomposition was examined through thermogravimetric analysis. Different compositions were prepared, as summarized in Table 1. The images of the photoresist before and after curing are illustrated in Figure S2. Owing to the better dispersion of MWCNTs, SCNT-PR1 and SCNT-PR2 showed an even and darker color compared with CNT-PR.

Table 1 Chemical composition of the MWCNTs nanocomposite photoresists

Sample group	IP-DIP (wt.%)	BDMP (wt.%)	Ac-MWCNT (wt.%)	PETMP (wt.%)
Control	100	0	0	0
CNT-PR	98.0	2	0.1	0
SCNT-PR1	87.9	2	0.1	10
SCNT-PR2	87.8	2	0.2	10

2.2 General procedure for the direct laser writing (DLW) process

A computerized 3D femtosecond (fs)-laser lithography instrument (Photonic Professional GT, Nanoscribe GmbH) was used to undertake the high-precision DLW process. Silicon wafers with an oxide surface layer (Si/SiO_2) were used as the printing substrate. Photoresist printing cells were first prepared (Figure S3(a)). In brief, the printing cells were prepared by stacking a glass slide (thickness: 0.7 mm, diameter: 15 mm) on top of the Si/SiO_2 substrate. The substrate and the glass slide were separated by a 100 μm thick Kapton tape. The modified photoresists were then infiltrated into the cells through a capillary effect. The DLW process was done in an oil configuration (Figure S3(b)). After the 3D printing process, the printing cell was opened, and the substrate was developed by immersing in poly(ethylene glycol) methyl ether acrylate (PEGMEA, Sigma-Aldrich) to remove the unpolymerized photoresist. Subsequently, the substrate was rinsed with 95% isopropanol (2-IPA), and a 365 nm, 6W UV lamp (Upland, USA) was used to illuminate the samples for the further polymerization of the microstructure. Finally, the sample was blow-dried using N2 gas. Different 3D computer-aided design (CAD) models were generated (Figure S3(c)) and converted into general writing language (GWL) using DeScribe (Nanoscribe GmbH, Germany), which defines the writing paths of the laser focus.

2.3 Printability study of the MWCNTs nanocomposite photoresist using DLW

Printability tests were conducted to determine suitable writing conditions of the MWCNTs nanocomposite photoresist for realizing complex 3D microstructures with good fidelity, which refers to the quality of the 3D printed structures in terms of shape, dimensions, and overall visual similarity to the intended structure [30]. First, the polymerization threshold of the photoresist was determined by coding a parametric sweep of different laser writing parameters using the software "DeScribe". A woodpile structure with overall dimensions of 20 µm × 20 µm × 20 µm (constructed of square rods 1 µm × 1 µm and a rod-to-rod spacing of 3 µm) was generated for the test. Laser power ranging from 10 - 35 mW and a writing speed of 5 - 10 mm/s were investigated. The optimal laser parameters were determined by the printing quality of the 3D woodpile microstructure through SEM observation. The range of laser energy dose for successful prints was calculated by the following equation:

$$Energy\ dose\ (J/\mu m) = Laser\ power\ (W)/\ writing\ speed\ (\mu m/s)$$

Subsequently, at the writing speed of 10 mm/s, the minimal laser power, i.e., the lowest laser power setting, was determined for generating metamaterials (Figure S3(c)) that can withstand the development step with good fidelity. Three metamaterials were generated with micron-sized truss members, the octet-truss micro-lattice, tetrakaidekahedron micro-lattice, and honeycomb structures [14], to determine suitable writing parameters. Further, at a writing speed of 10 mm/s and minimal laser power setting, the minimum feature size of this laser parameter was determined by constructing a woodpile structure with rods generated by a single printing path for defining the printing resolution (line-to-line spacing of 2 µm).

2.4 Study of the susceptor-assisted microwave pyrolysis (SMWP) conditions

Pyrolysis of the photocured IP-DIP photoresist was first undertaken to investigate the effects of the susceptor-assisted microwave pyrolysis (SMWP) conditions on the properties of the PyC product. The SMWP was conducted in a commercial single-mode 2.45 GHz MW furnace (HAMiLab-HV3000, Synotherm, China). The samples were placed inside the kiln, made of alumina (Al_2O_3, 18 mm thick) with an inner layer of silicon carbide (SiC, 2 mm thick), and the furnace chamber was vacuumed and purged with N_2 gas. Afterwards, the SMWP process was initiated. According to the degradation profile of the photoresist, the fully automated protocol was divided into two stages. In the first stage, the specimens were heated from room temperature to 450 °C for 10 mins at a heating rate of 10 °C/min. The second heating stage started at 450 °C, and a fixed heating rate of 20 °C/min to the target temperature was set. The MW power was adjusted automatically from 100 W to 400 W to match the heating profile. Throughout this study, all samples were heat treated using the same heating rate profile. The processing conditions studied are summarized in Table 2. After the SMWP process, the specimens were allowed to cool down in the MW furnace to room temperature. The effects of SMWP conditions on the properties of the PyC product were investigated. Moreover, the properties of PyC fabricated by conventional pyrolysis (CP_IPT8D3) were compared to study the effectiveness of the SMWP. This was done using a tube furnace (Carbolite Gero, UK) with the same heating profile as the SMWP process. In brief, the tube furnace was programmed to reach and maintain a temperature of 800 °C for 30 min at a heating rate of 20 °C/min. The temperature inside the tube was monitored using a built-in thermocouple and the heating was conducted under N_2 atmosphere. The pyrolysis condition that resulted in better electrical and electrochemical performance of the pyrolytic product was selected for processing the MWCNTs nanocomposite photoresist for further investigation.

Table 2 Processing conditions for the pyrolysis process of IP-DIP photoresist

	Sample	Heating rate at >450 °C (°C/min)	Target temperature (°C)	Dwell time (min)
SMWP	IPT6D3	20	600	30
	IPT7D3		700	
	IPT8D3		800	
	IPT8D1	20	800	10
	IPT8D5			50
Conventional pyrolysis	CP_IPT8D3	20	800	30

2.5 Characterization

Transmission electron microscopy (TEM, JEOL-2011) was used to examine the morphology of the MWCNTs before and after the surface modification process. A scanning electron microscope (SEM) equipped with an energy-dispersive X-Ray (EDX) spectroscopy (JEOL JSM-6490) was employed for morphological and elemental characterizations. Fourier-transform infrared (FTIR) analyses were conducted using an FTIR spectrometer (Bruker Vertex-70) with the KBr pellet method. Prior to the characterization, the KBr sample was vacuum dried at 80 °C for 4 hours and was stored in a nitrogen (N2) filled vacuum desiccator overnight for complete water removal. The spectra of the samples were obtained from 16 scans within the wavenumber range of 500 - 4000 cm^{-1} with a resolution of 4 cm^{-1}. The thermal stability of the MWCNTs and the as-prepared photoresists were investigated through thermogravimetric analysis (TGA) using a thermogravimetric instrument (Mettler Toledo TGA/DSC3+), scanned at a temperature ranging from room temperature to 800 °C at a heating rate of 20 °C/min under an N_2 atmosphere. The choice of using the same heating rate as the pyrolysis process was made to ensure alignment between the TGA and the pyrolysis process, thereby maintaining the relevance of the result. UV-VIS spectroscopy was conducted using a UV-Vis

spectrometer (Perkin Elmer Lambda 650, USA) to evaluate the absorbance of the unpolymerized photoresists.

Raman microspectroscopy was employed for characterizing the PyC atomic structures using a micro-Raman Spectrometer (LabRAM HR 800, grating: 1800 g/mm). Disc-shaped samples (diameter of 50 µm and thickness of 5 µm) were prepared by DLW and subjected to pyrolysis process. A laser beam with 488 nm wavelength at 50 mW laser power was used as an excitation source. Each sample was scanned within the region of 1000 cm^{-1} - 3200 cm^{-1}. The degree of structural disorder of the carbon after pyrolysis of the polymer precursor was assessed by the intensity ratio between the D peak and G peak, i.e., I_D/I_G.

2.6 Electrical and electrochemical performance

2D electrode chips were prepared by photopatterning to study the effect of SMWP conditions on the electrical and electrochemical performance of the pyrolyzed samples, as illustrated in Figure S4. A photoresist cell was prepared using a Kapton tape spacer of 30 µm thickness with a PET film covering the top. Two photomasks were used. A photomask with a square area of 25 mm^2 with four electrode contacts at each corner was employed for electrical measurement. While for the electrochemical analysis, the photomask consisted of a circular pattern (area = 12.6 cm^2) with a wick (5 mm long and 0.75 mm wide). The pattern transfer was done using a 365 nm 6W handheld UV lamp (Upland, USA), and the exposed area was photopolymerized. Subsequently, the PET film was lifted off, and the 2D pattern was developed, followed by SMWP at different conditions.

The electrical properties of the samples were investigated by the four-point probe method using a probe station (The Micromanipulator Co., USA) equipped with a Keithley 4200a-

SCS parameter analyzer (Tektronix, USA). The bulk resistivities (ρ) of the PyC samples prepared from different SMWP conditions and the SCNT-PR1-derived PyC, denoted as PyC_CNT, were determined based on the following equation:

$$\rho = \frac{V}{I}\frac{\pi t}{\ln(2)}$$

where V = applied current, I = measured voltage, and t = thickness of the sample.

The electrochemical performance of the sample was characterized using cyclic voltammetry (CV) and electrochemical impedance spectroscopy (EIS). The measurements employed a three-electrode configuration and were conducted using a CHI6600 electrochemical workstation (Shanghai Chenhua, China). A ferri-ferrocyanide redox couple $[Fe(CN)_6]^{3-/4-}$ redox couple was used. All electrochemical measurements were performed in 0.5 M potassium chloride (KCl) solution (Fuchen, China) containing 10 mM potassium ferricyanide ($K_3Fe(CN)_6$, Aladdin, China). The scans were performed at a potential ranging from -0.3 V to 0.9 V for the CV test, and at least six cycle scans were obtained to ensure reproducibility. Different scan rates ranging from 10 – 100 mV/s were employed to study the electrochemical behavior of the PyC electrodes. The impedance data were acquired by applying a 5 mV AC potential with frequencies ranging from 0.1 – 10^5 Hz.

3 Results and discussion

3.1 Pyrolysis behaviors of the MWCNTs nanocomposite photoresist

The TGA of the MWCNTs samples was first recorded, as presented in Figure 2(a). The as-received MWCNTs demonstrated better thermal stability with minimal weight loss of <10 % below 600 °C, while a significant weight loss was measured for Ac-MWCNTs and S-MWCNTs for over 20 % and 45 %, respectively. The increase in weight loss was

due to the grafting of functional groups on the MWCNTs after the two-step functionalization. For Ac-MWCNTs, there was a slight reduction in weight at a temperature around 100 °C, possibly attributable to the initial degradation of carboxyl and hydroxyl functional groups [31] and the removal of the impurities, such as water or oxygen, introduced after the acid treatment. For S-MWCNTs, a significant mass loss of over 47 % at 300 - 500 °C was recorded for the decomposition of the thiol molecule (Figure 2(b)).

The pyrolysis behavior of the cured MWCNTs photoresists was also assessed, and the maximum mass loss temperature (T_{max}) was determined, which is the decomposition temperature and is crucial for determining the minimum temperature for the pyrolysis process. The CNT-PR was not considered because of the poor dispersibility of the MWCNTs. Figure 2(c) shows similar degradation profiles for the photoresist samples, with major weight loss starting at 350 °C. At above 350 °C, polymer chain rearrangement occurred, followed by vaporization to eliminate the heteroatoms from the polymer, leading to a significant mass loss. At over 600 °C, the weight loss for all samples slowed down. While at 800 °C, the solid residue amount of IP-DIP, SCNT-PR1, and SCNT-PR2 were 1.7%, 3.6%, and 5.4%, respectively, due to the increased MWCNTs content. The thermal stability of the photoresist was also improved by adding MWCNTs. From the DTG result (Figure 2(d)), a higher T_{max} for both SCNT-PR1 and SCNT-PR2 (461 °C) was recorded as compared to IP-DIP (450 °C), indicating a higher thermal degradation resistance.

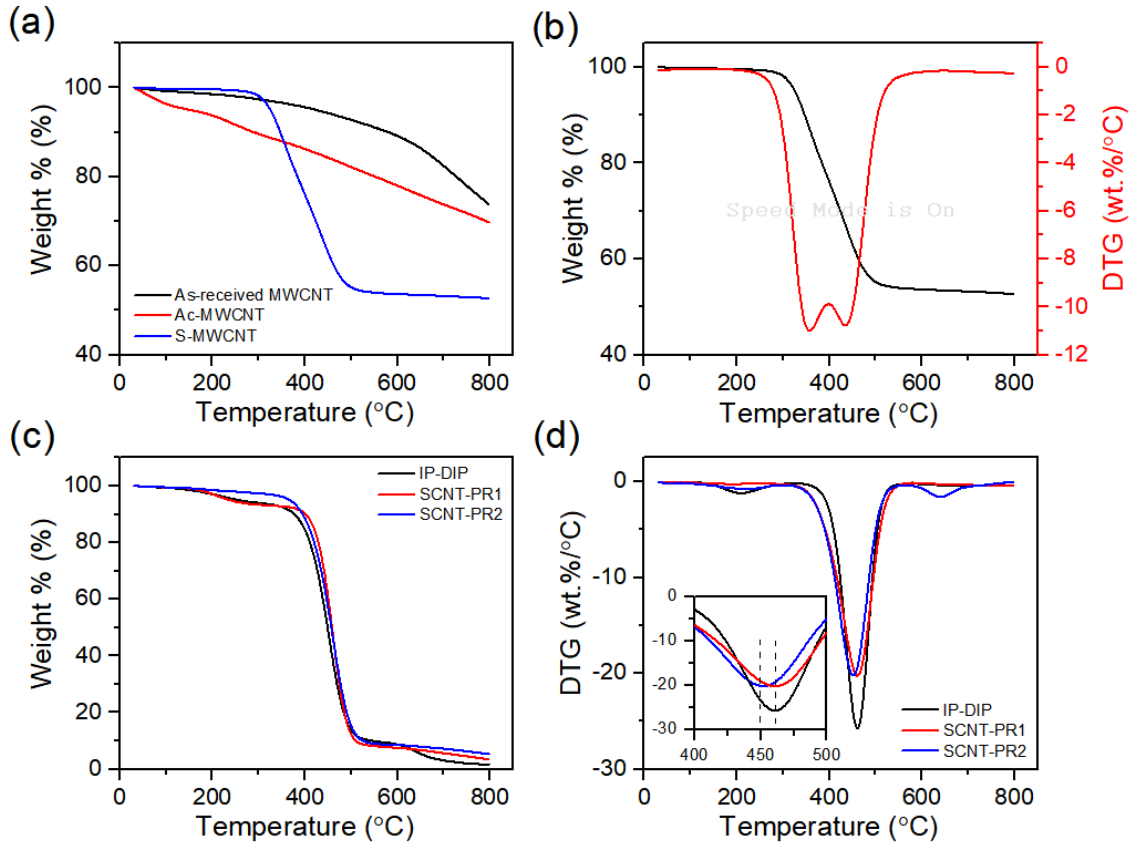

Figure 2(a) TGA of the as-received MWCNTs, Ac-MWCNTs, and S-MWCNTs and (b) DTG curve of S-MWCNTs. (c) TGA and (d) DTG analysis MWCNTs photoresists with different compositions

3.2 UV-VIS spectra

The optical absorption of the MWCNTs nanocomposite photoresists was studied using UV-VIS spectroscopy, as displayed in Figure 3. After the addition of S-MWCNTs, the optical absorption of the photoresists throughout the entire spectrum increased. Moreover, a strong absorption at 420 nm was also recorded due to the existence of the photoinitiator. As the DLW employed a two-photon polymerization mechanism, good absorption at λ/2 (i.e., 390 nm) was conducive to effective photopolymerization during 3D printing.

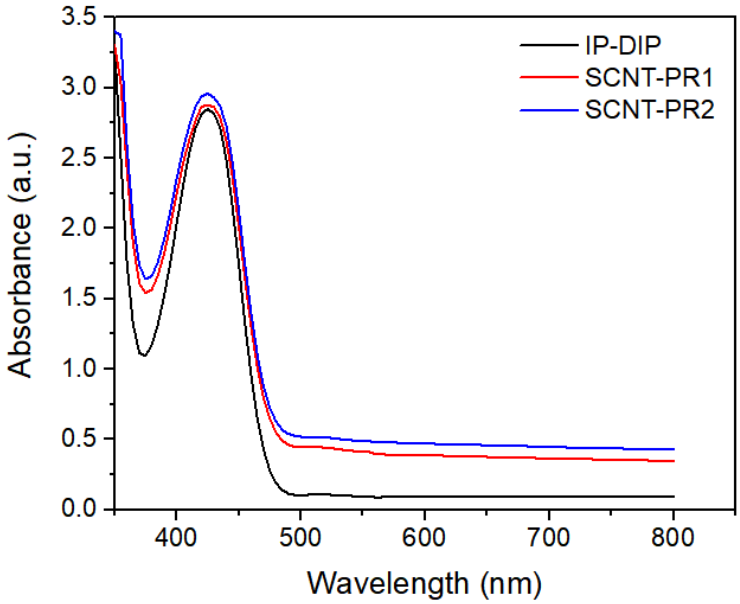

Figure 3 The UV-Vis spectrum of IP-DIP, SCNT-PR1, and SCNT-PR2

3.3 Printability assessment for the MWCNTs nanocomposite photoresist

The intrinsic two-photon polymerization mechanism of DLW has rendered it as a powerful tool for true 3D additive manufacturing. In comparison to other 3D printing technologies, DLW enables the precise fabrication of intricate 3D microstructures with nanoscale resolution (Figure S5). To enhance printing quality using the newly developed photoresist, a series of printability tests were conducted to identify suitable printing parameters and determine the line resolution

Study of DLW conditions

Printability assessment was conducted to investigate the most suitable DLW condition for SCNT-PR1 photoresist. The SEM images in Figure 4 show the woodpile structures produced with IP-DIP and SCNT-PR1 at different laser writing conditions. Based on the fidelity of the microstructures, the range of successful prints is highlighted in red area. For IP-DIP (Figure 4(a)), the lowest laser setting was found at laser power = 15 mW and writing speed = 5 mm/s. As the exposure time was shorter, i.e., the writing speed

increased, higher laser power was needed to initiate and sustain the photopolymerization. However, as laser power >30 mW, the excess energy dose caused the formation of larger voxels during the printing, which reduced the quality of the structure as a result of overexposure. [32]. It was also observed that the minimum laser power increased for an increasing writing speed, due to the minimum energy required to attain the polymerization threshold during the printing process. From the printability test for IP-DIP, it was calculated that the laser energy dose required for successful printing within the tested range falls within $2.5 \times 10^{-6} – 5 \times 10^{-6}$ J/μm.

For SCNT-PR1 (Figure 4(b)), a lower polymerization threshold was observed with a lower laser power setting at 10 mW at a writing speed of 5 mm/s. This phenomenon is attributed to the presence of thiol molecules with different photopolymerization mechanisms. First, thiol molecules can reduce oxygen inhibition during acrylate photopolymerization [33]. As the presence of oxygen may hinder the propagation reaction of the photoresist, adding thiol molecules can reduce the excited state quenching of the photoinitiator during photopolymerization. In addition, the thiol molecules also involved in a thiol-ene radical reaction, illustrated in Figure 4(c). As the photoinitiator (I) is excited by the fs-laser through two-photon absorption, a thiyl radical is formed, which it propagates through the C=C bond of the acrylate monomer. A series of reactions are initiated, including (1) chain-transfer reaction between the polymer radicals and the thiol molecule, (2) propagation reaction through another acrylate monomer, and (3) termination reaction by radical–radical recombination. The thiol-ene photopolymerization shows a faster reaction rate than the radical-based photopolymerization involving acrylates [34]; as a result, a lower energy threshold is observed. In addition, it has been reported that the thiol molecules also improve the photo-reactivity of the photoresist, which is beneficial to formulating photoresists with better

processability [35]. The improvement is due to the reduced oxygen inhibition by the thiolation, and the step-growth polymerization reaction mechanism reduces the structural shrinkage during the photopolymerization owing to the homogeneous crosslinked network. A more efficient photopolymerization with higher conversion can also be achieved. This is further supported by the lower energy dose required to achieve successful prints for SCNT-PR1, falling within the range of $1.5 \times 10^{-6} - 4 \times 10^{-6}$ J/μm. Further increases in laser power to 25 mW resulted in lower printing quality of the structure, as observed in the SEM image. Moreover, laser power increase is needed for higher writing speed in order to achieve good structure quality. Table 3 summarizes the suitable range of laser writing parameters DLW for IP-DIP and SCNT-PR1.

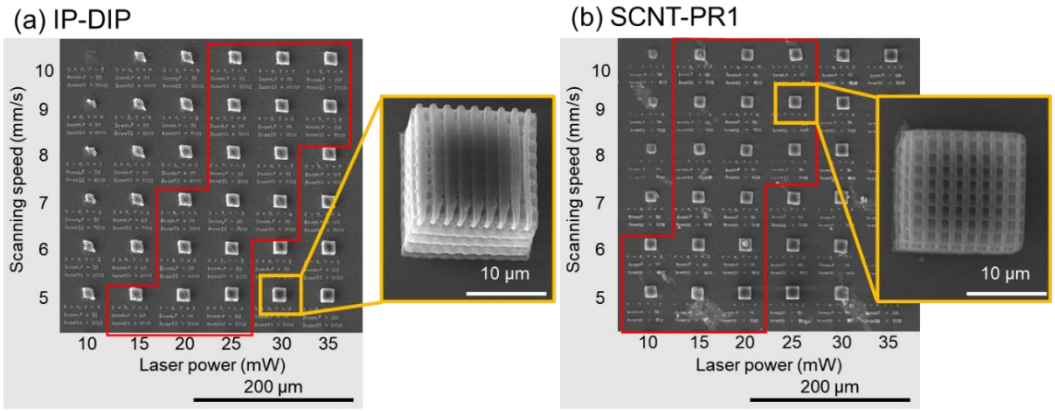

(c) Initiation:

$$I \xrightarrow{hv} 2\,R\cdot$$
$$R\cdot + R-SH \rightarrow R-S\cdot$$

Propagation:

$$R-S\cdot + R'CH=CH_2 \rightarrow R'C\cdot H-CH_2-SR$$
$$R'C\cdot H-CH_2-SR + R-SH \rightarrow R'CH_2-CH_2-SR + R-S\cdot$$

Termination:

$$2R'C\cdot H-CH_2-SR \rightarrow \begin{matrix} R'CH-CH_2-SR \\ | \\ R'CH-CH_2-SR \end{matrix}$$
$$2R-S\cdot \rightarrow R-S-S-R$$
$$2R'C\cdot H-CH_2-SR + R-S\cdot \rightarrow \begin{matrix} R'CH-CH_2-SR \\ | \\ S-R \end{matrix}$$

Figure 4 SEM images of a 9 × 9 array of woodpile structures using (a) IP-DIP and (b) SCNT-PR1. Red areas represent the range of successful prints with good fidelity and

without defects. Enlarged images for structures both within and out of this range are also shown. (c) The thiol-ene photopolymerization reaction mechanism.

Table 3 Summary of DLW conditions for producing structures with good fidelity.

Laser writing speed (mm/s)		**5**	**6**	**7**	**8**	**9**	**10**
Laser power (mW)	**IP-DIP**	15 - 25	20 - 25	20 - 30	25 - 30	25 - 35	25 - 35
	SCNT-PR1	10 - 20	10 - 20	15 - 20	15 - 25	15 - 25	15 - 25

Minimal laser writing condition for 3D metamaterials at the highest writing speed

Based on the above finding, the highest writing speed at 10 mm/s was selected for further investigation to reduce the printing time of the microstructures. To obtain the most suitable writing condition for producing complex 3D metamaterials with good fidelity, an individual printing test was performed for each structure, and the minimal laser power was determined. Three sets of printing for each metamaterial were undertaken to ensure repeatability, and the SEM images are shown in Figure 5. As observed, good-quality structures were fabricated within the range of laser conditions found in the printability assessment. The minimal laser power was found at 25 mW for IP-DIP, and all metamaterials showed good structural integrity and fidelity after the development process (Figure 5(a)). In comparison, SCNT-PR1 showed a lower minimal laser power at 15 mW due to a reduced polymerization threshold in the presence of thiol molecules (Figure 5(b)).

Line resolution at minimal laser writing conditions

Different laser settings affect the voxel size formed during the DLW process, thereby affecting the line resolution of the microstructure. The line resolution of SCNT-PR1 was assessed by printing a woodpile structure constructed with rods generated by a single printing path at the minimal laser power of 10 mm/s. The line width on the top layer was determined and is shown in Figure 5(c). The resolution of the IP-DIP photoresist can reach as high as 150 nm (Figure S6), according to the manufacturers' data. After

modification with S-MWCNTs, the SCNT-PR1 photoresist showed a significant increase in the line resolution, reaching 833 ± 54 nm. During the laser writing process, localized heat was generated due to the exothermal nature of photopolymerization [36]. The formation of excess thiyl radicals are initiated through a thermal free-radical reaction [37]. This lead to the "dark reaction", where the excess thiyl radicals diffuse and propagate to the unreacted photoresist outside the laser spot [35]. Larger voxels can be created during the printing process, however, despite the reduction in the line resolution, are still within the submicron regime (<1μm). Besides, smooth surfaces were observed on the rods of the woodpile structure, no CNTs protruding from the surface. This is probably attributable to the self-alignment of CNTs along the laser scanning direction, influenced by spatial confinement, volume shrinkage of the structures, and optical gradient force [38, 39].

Stability of overhanging structures at minimal laser writing conditions

During the DLW process, unsupported portions of the structures may exhibit plastic deformation either due to residual stress after the development process or self-buckling. Therefore, micro-bridges were fabricated at the minimal laser writing condition. The length span of laser-printed overhanging structures without obvious deformation was examined. Two-end supported beam structures with a cross-section of 5 μm (W) × 7 μm (H) and an unsupported length ranging from 60 μm to 120 μm were produced (Figure 5(d)). For the IP-DIP photoresist, significant deformation was observed for the unsupported portion of all printed structures. In contrast, no deformation was observed for the structures fabricated using SCNT-PR1, owing to the enhanced stiffness by adding the MWCNTs [38]. The results provide valuable information for designing complex 3D structures with overhang components.

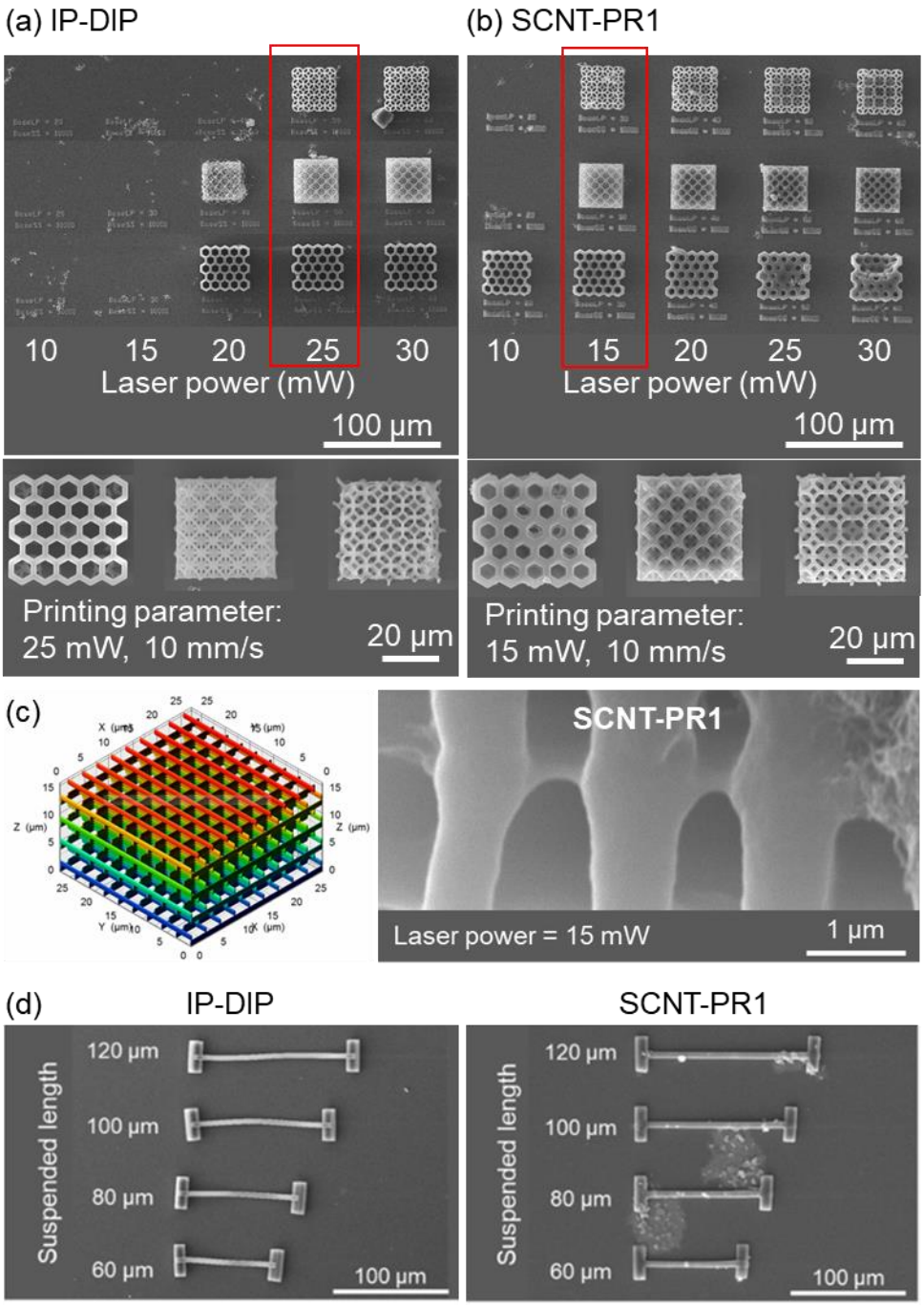

455

456 Figure 5 Minimal laser power for producing metamaterials at a fixed scanning speed of

457 10 mm/s: (a) IP-DIP and (b) SCNT-PR1. (c) Line resolution of SCNT-PR1 at minimal

458 laser power and scanning speed of 10 mm/s. (d) SEM images of micro-bridges

459 fabricated

460

3.3 Fabrication of 3D PyC-based metamaterials

DLW technology possess great potential to mitigate material defects due to its capability to produce structure with submicron resolution and reducing the overall size of geometrical features [13]. Three metamaterials were generated by the DLW technology and subsequently converted to 3D PyC metamaterials through the SMWP process. A supporting structure was employed underneath the metamaterials to minimize the substrate effect that restricts the structural shrinkage during the pyrolysis. The polymer-based 3D metamaterials were successfully transformed into PyC-based metamaterials through the SMWP at 800 °C for 30 min. The SEM images in Figure 6(a) reveal the 3D PyC-based microstructures of IP-DIP and SCNT-PR1 after pyrolysis, where the IP-DIP and SCNT-PR1 microstructures shrank almost isotropically after pyrolysis, suggesting the substrate effect was reduced. With the aid of a supporting structure, the degassing process during pyrolysis can take place in any direction, therefore, an isotropic shrinkage can be achieved. The IP-DIP-derived PyC microstructures showed a substantial shrinkage of over 75% in width after pyrolysis. After the pyrolysis, the structures almost lost geometrical details due to the considerable shrinkage, highlighting the critical challenge of preserving intricate geometrical features.

SCNT-PR1 3D metamaterials underwent the SMWP at the same pyrolysis condition (Figure 6(b)). Unlike the IP-DIP-derived PyC microstructures, all the SCNT-PR1-derived PyC microstructures shrank only by ~55% in width. As MWCNTs are thermally stable and hardly to be decomposed at the pyrolysis temperature [40], the additional of MWCNTs improved the shrinkage resistance of the SCNT-PR1 metamaterials, which is crucial for avoiding defects such as cracks and delamination. This is also proven by the higher amount of solid residual formed from the SCNT-PR1at 800 °C according to the TGA result (Figure 2(c)). After pyrolysis, these PyC structures can be potentially used as

microelectrodes for advanced technologies such as biosensors [41] and electrochemical MEMS devices [42].

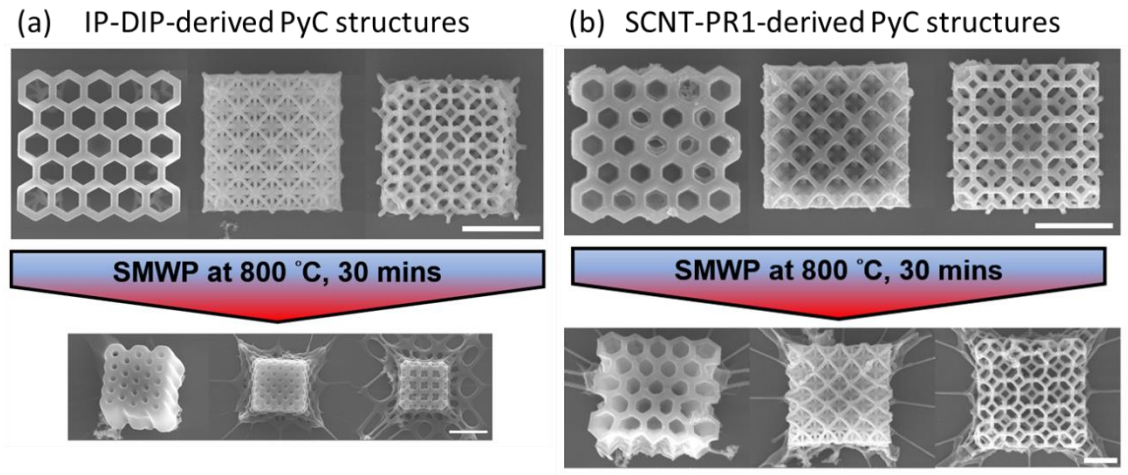

Figure 6 SEM images of (a) the IP-DIP metamaterials produced by DLW before (scalebar = 20 µm) and after pyrolysis through the SMWP (scalebar = 5 µm), and (b) SCNT-PR1 metamaterials produced by DLW before (scalebar = 20 µm) and after pyrolysis through the SMWP (scalebar = 5 µm)

3.4 Effects of SMWP conditions on the atomic structure of the PyC products

The effects of conditions in the SMWP process, including pyrolysis temperature and dwell time, were studied. The degree of disorder in the atomic structure of the PyCs produced from IP-DIP was investigated by Raman spectroscopy. Two distinctive peaks around 1350 cm^{-1} and 1580 - 1600 cm^{-1} were identified for the PyC samples after the pyrolysis, corresponding to the D peak (disordered band) and the G peak (originated from the graphitic structure). For better interpretation, the Raman spectra were normalized to the G peak, and the D to G peak intensity ratio, i.e., I_D/I_G was estimated. Figure 7(a) shows the Raman spectra for the IP-DIP-derived PyC samples fabricated at different temperatures through the SMWP. From the normalized spectra, D peak intensity increased with the pyrolysis temperature, similar to the characteristics of the glassy

carbon annealed at elevated temperatures [43]. As a result, an increasing I_D/I_G is observed. Understanding the evolution of the graphitic crystallites during the pyrolysis process is crucial for interpreting the properties of the pyrolytic product. In the case of the amorphous carbon annealed at elevated temperatures, the D peak broadening is due to the formation of sp^2-bonded clusters [44]. In contrast, an increase in bandwidth with a decrease in peak intensity indicates the formation of non-sixfold rings. Therefore, for amorphous carbon materials annealed at higher temperatures, the formation of a more ordered carbon atomic structure displays an increase in the D peak intensity. During pyrolysis, polymer fragmentation and rearrangements of carbon atoms take place. More sp^2 carbons and ordered aromatic rings are formed, and the sp^2 cluster size increases. For PyC samples derived from IP-DIP, the ratio of I_D/I_G increased from 0.72 to 0.90 as the processing temperature increased from 600 (IPT6D3) to 800 °C (IPT8D3). This implied the formation of more aromatic rings and led to a more ordered carbon atomic structure. The second-order peaks, including the 2·D1 (~2695 cm^{-1}) and G+D1 peaks (~2960 cm^{-1}) (inset of Figure 7(a)) were also investigated. The decreased 2·D1 peak intensity in the normalized Raman spectrum suggested an increase in the stacked graphene layers, a useful trait for comparing the atomic structure of the PyCs [43]. As observed, the increasing pyrolysis temperature decreased the 2·D1 peak intensity, suggesting increased layers in the stacked graphite domains within the PyC. The G+D1 peak is another characteristic of the carbon atomic structure, representing the forbidden combinations mode due to the disordered carbon [45]. The G+D1 peak intensity showed a similar trend to the 2·D1 peak as the pyrolysis temperature increased, suggesting the formation of larger graphite crystalline domains. From the results, the IP-DIP-derived PyCs became less disordered as the processing temperature increased.

529 The effect of dwell times on the IP-DIP-derived PyC produced through the SMWP at 800
530 °C was also investigated. The Raman spectra of the samples pyrolyzed for 10 (IPT8D1),
531 30 (IPT8D3), and 50 (IPT8D5) min are shown in Figure 7(b). A slight increase in the D
532 peak intensity was observed for IPT8D3 compared with IPT8D1, indicating the formation
533 of less distorted aromatic rings. However, the carbon atomic structure between IPT8D3
534 and IPT8D5 showed a similar degree of disorder, as proven by the same I_D/I_G value. In
535 addition, similar 2·D1 and G+D1 peak intensities were observed. The result suggested
536 that more ordered aromatic rings were formed during the first 30 min of the SMWP.
537 However, the processing time was less significant in forming a larger stacked graphite
538 crystalline domain.
539 Figure 7(c) shows the Raman spectra of IP-DIP-derived PyC produced at the same
540 processing condition (i.e., 800 °C for 30 min) through the SMWP (IPT8D3) and the
541 conventional heating (CP_IPT8D3). As observed, an increase in the D peak intensity and
542 a slight decrease in G+D1 peaks were recorded for the IPT8D3. The I_D/I_G values for
543 IPT8D3 and CP_IPT8D3 were 0.90 and 0.80, respectively. The results showed that the
544 SMWP can facilitate the formation of a less disordered carbon atomic structure with a
545 larger graphite crystalline domain, which may be attributed to the intrinsic heating
546 mechanism of the susceptor-assisted microwave process, leading to an accelerated
547 pyrolysis reaction [27].
548 The Raman characteristics of the SCNT-PR1-derived PyCs, i.e., PyC_CNT, were also
549 studied, as presented in Figure 7(d). The I_D/I_G value for the IPT8D3 was 0.90, while for
550 PyC_CNT, a lower I_D/I_G value of 0.83 was recorded. The decreases in I_D/I_G for
551 PyC_CNT were due to the increased fraction of graphitized carbon after pyrolysis due to
552 the existence of the thermally stable MWCNTs. Therefore, a more ordered carbon atomic
553 structure was obtained. Besides, adding MW-absorbing CNTs lead to a more efficient

pyrolysis reaction under MW irradiation. Table 4 summarizes the D and G peaks' position, and the I_D/I_G values for all the samples.

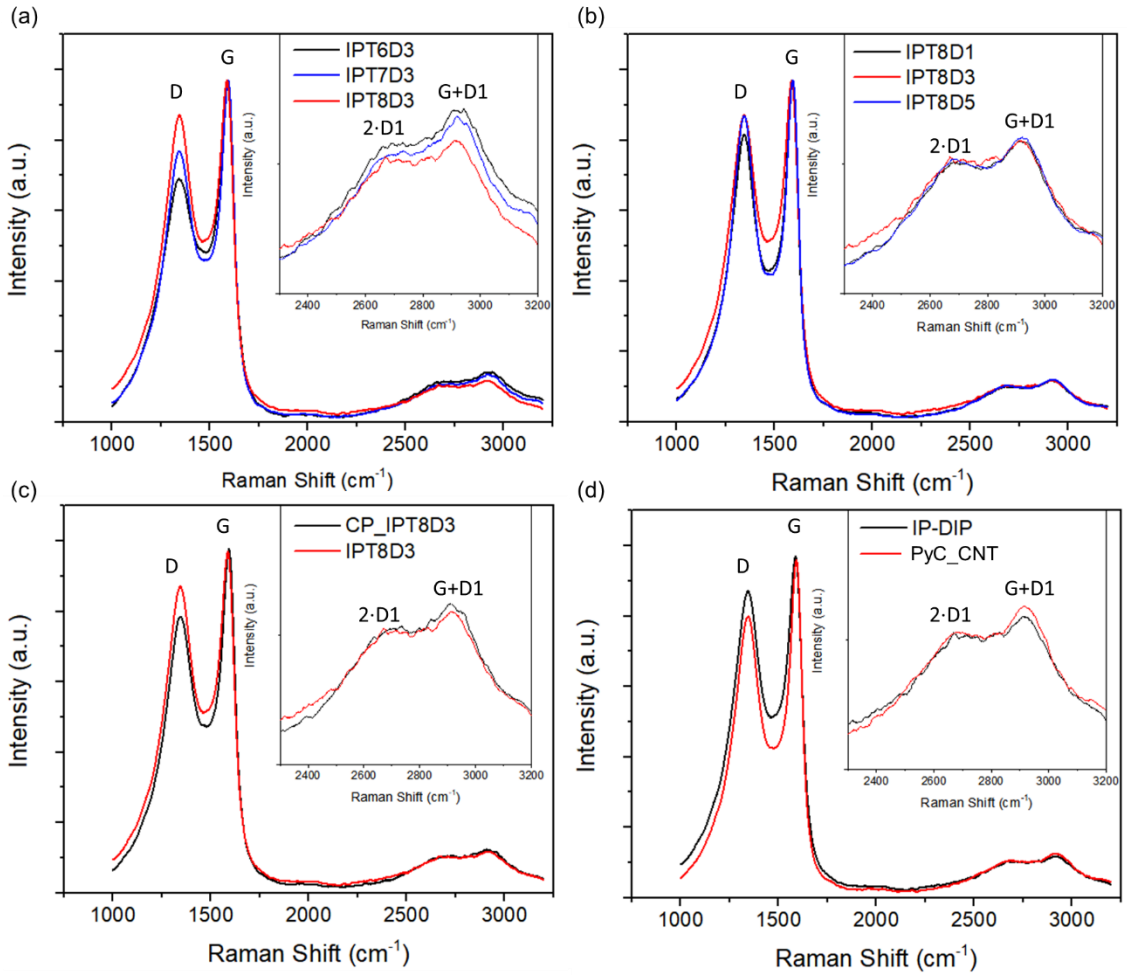

Figure 7 Raman spectra of IP-DIP-derived PyCs obtained at different (a) temperatures (dwell time: 30 min) and (b) dwell times (pyrolysis at 800 °C); (c) IP-DIP-derived PyC using obtained at 800 °C with a dwell time of 30 min through the SMWP and conventional heating; (d) PyC_CNT obtained at same SMWP condition.

562 Table 4 I_D/I_G ratios in Raman spectra of PyCs under different processing conditions

PyC Samples		D band Position (cm^{-1})	G band Position (cm^{-1})	I_D/I_G
IP-DIP-derived PyC	IPT6D3	1343	1588	0.72
	IPT7D3	1342	1593	0.79
	IPT8D3	1345	1588	0.90
	IPT8D1	1345	1592	0.85
	IPT8D5	1344	1592	0.90
	CP_IPT8D3	1345	1593	0.80
PyC_CNT		1345	1590	0.83

563

564 **3.5 Effects of MW pyrolysis on the electrical and electrochemical properties**

565 The electrical properties of the IP-DIP-derived PyC fabricated under different pyrolysis
566 conditions were investigated. Figure 8(a) presents the resistivity values for the PyC films
567 produced at different temperatures through the SMWP. As the temperature increased
568 from 600 °C to 800 °C, a significant reduction in the resistivity of the PyC film was
569 recorded. The PyC sample IPT6D3 showed a resistivity of 54.20 ± 7.27 Ω cm. As the
570 pyrolysis temperature reached 800 °C, the PyC sample IPT8D3 showed a drastic decrease
571 in resistivity to 0.16 ± 0.01 Ω cm, a two-order of magnitude reduction compared to 700
572 °C. During pyrolysis at high temperatures, a series of pyrolytic reactions occurred, and
573 the impurities and heteroatoms, such as oxygen and hydrogen, were removed from the
574 polymer through vaporization [46]. At above 600 °C, more aromatic hydrocarbon
575 molecules and fragmented graphene were formed [47]. At a higher pyrolysis temperature,
576 the rearrangement of the carbon atomic structure reduced the defects in the carbon
577 structure and facilitated the growth of the graphene domain. As a result, a substantial
578 decrease in the resistivity of the PyC film was recorded, a conclusion also supported from
579 the findings in the Raman spectra analyses.

We also compared the resistivity value of the PyC films obtained through conventional pyrolysis at the same processing condition. The PyC sample CP_IPT8D3 showed a resistivity value of $0.69 \pm 0.13\ \Omega$ cm. In comparison, the resistivity of IPT8D3 fabricated through the SMWP was reduced by almost 75%, mainly ascribed to the accelerated reaction kinetics with lower activation energy under MW pyrolysis than conventional heating [27]. The SMWP can improve pyrolysis process and enhance the resistivity of the PyC, achieving higher overall effectiveness of the process.

Figure 8(b) presents the resistivity of the IP-DIP-derived PyC fabricated under different dwell times. At 800 °C, a decreasing trend of the resistivity of the PyC samples was confirmed as the dwell time increased. The highest resistivity of $36.62 \pm 12.84\ \Omega$ cm was recorded for IPT8D1(dwell time = 10 min), while the resistivity greatly decreased to 0.16 $\pm$ 0.01 Ω cm for IPT8D3 (dwell time = 30 min), and then slightly decreased to 0.14 $\pm$ 0.02 Ω cm for IPT8D5 (dwell time = 50 min). The dwell time for pyrolysis has a considerable impact on the electrical conductivity of the PyC product. Prolonged pyrolysis allowed more time for the rearrangement of the carbon atoms and the formation of more ordered aromatic rings [48]. As a result, the conductivity was improved, also proven by the findings from the Raman spectra analysis of the PyC samples.

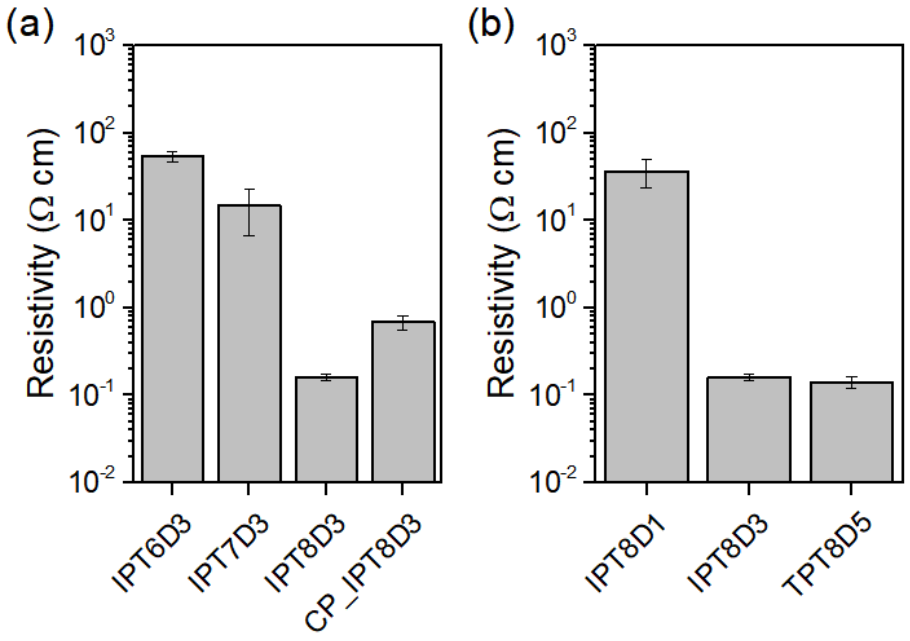

Figure 8 Resistivity of IP-DIP-derived PyC films produced through SMWP and conventional heating at (a) different pyrolysis temperatures and (b) dwell time.

Cyclic Voltammetry (CV) was employed to study the influences of different processing conditions under the SMWP on the electrochemical properties of the PyC product derived from the IP-DIP. The redox reaction characteristics of the electrochemical cell, e.g., the reversibility, electron transfer, and the interaction between the PyC working electrode and the electrolyte, were analyzed. Figure 9(a) shows the CV voltammograms of PyC samples produced at different temperatures through the SMWP using IP-DIP. For the PyC samples prepared below 800 °C (i.e., IPT6D3 and IPT7D3), no redox peaks were observed due to the high electrical resistivity working electrode. For IPT8D3, distinctive cathodic (i_{pc} = -0.271 mA) and anodic peak currents (i_{pa} = 0.271 mA) of the same magnitude were recorded, with peak-to-peak potentials (ΔE_p) of 98 mV.

The electrochemical behavior of the IPT8D3 PyC sample was further studied. CVs at different scan rates (v), ranging from 10 mV/s to 100 mV/s, were applied to assess the reversibility of the electrochemical reaction (Figure 9(b)). The recorded i_{pa} and i_{pc} were equal at all scan rates, and the magnitude increased with the scan rate. When the scan rate

increased, a higher step potential was applied within a shorter period. As a result, a thicker electric double layer was formed, and the electric flux reduced. Therefore, the peak currents increased with the scan rate. The lowest ΔE_p was recorded at 10 mV/s with a value of 66 mV, which approaches the theoretical Nernstian behavior (~59 mV) of the $[Fe(CN)_6]^{3-/4-}$ redox reaction. The relation between the peak currents and the square root of the scan rate is shown in Figure 9(c) for studying the mass transport kinetics of the electrochemical cells using the IPT8D3 PyC working electrode, and a linear correlation was observed. According to the Randles-Sevcik equation, the electrochemical behavior of the IPT8D3 PyC working electrode is a diffusion-controlled process, similar to the glassy carbon produced by the conventional pyrolysis process [42, 49].

EIS was also employed to examine the electrochemical behavior of the IPT8D3 PyC electrode. The sample produced through conventional heating (CP_IPT8D3) was studied for comparison. The Nyquist plots for IPT8D3 and CP_IPT8D3 are shown in Figure 9(d), and the data are fitted using the Randles equivalent circuit models. As shown in the figure, both samples showed a similar shape in the Nyquist plot. At the high-frequency range, a semicircle was formed, representing the electron transfer kinetics, while a linear portion shown in the low-frequency region represents the diffusion-limited process. The electrolyte resistance (R_{sol}) and charge transfer resistance (R_{ct}) of the electrochemical cell were calculated, where R_{sol} is independent of the electrode properties as proven by the similar value after fitting. IPT8D3 showed a smaller semicircle, corresponding to a lower R_{ct} of 206.0 ± 56.6 Ω compared to 822.3 ± 41.5 Ω for CP_IPT8D3. The lower R_{ct} for IPT8D3 indicated a better electron transfer and lower electrochemical reaction rate for the redox couple compared to the samples prepared by conventional oven pyrolysis [50].

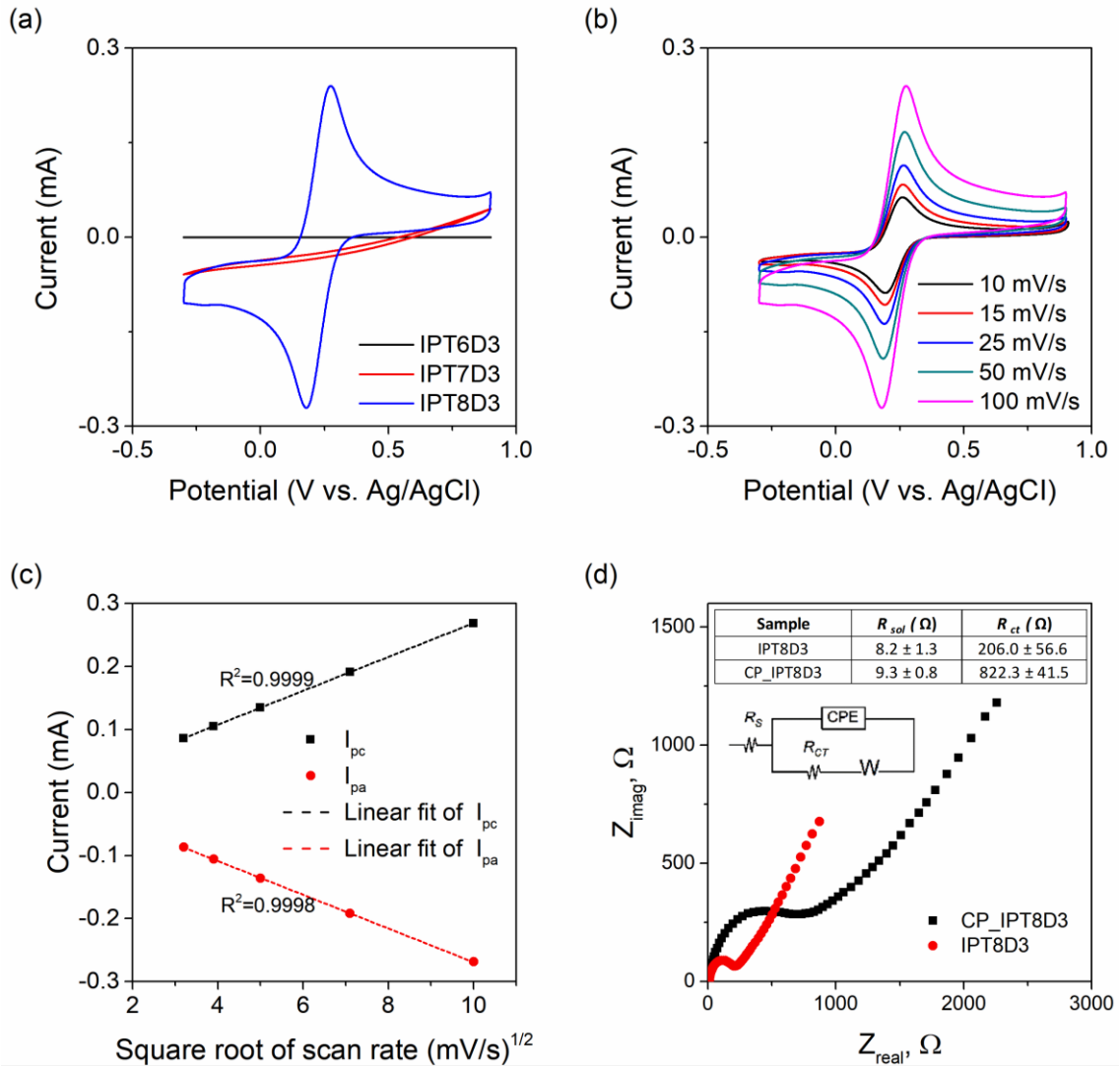

Figure 9 (a) Voltammograms of IP-DIP-derived PyC obtained at different pyrolysis temperatures (dwell time: 30 min) through the SMWP. (b) Voltammograms of IP-DIP derived PyC obtained at 800 °C (dwell time of 30 min) with varying scan rates and (c) linear correlation between the peak currents and the square root of scan rate. (d) Impedance spectra of IP-DIP-derived PyC fabricated through conventional heating (CP_IPT8D3) and SMWP (IPT8D3).

3.6 Electrical and electrochemical properties of SCNT-PR1-derived PyC

From the above results, the IP-DIP-derived PyC samples fabricated at 800 °C for 30 min through the SMWP showed enhanced electrical and electrochemical properties. The same processing condition was chosen for the pyrolysis of the SCNT-PR1 photoresists, and PyC_CNT was obtained after pyrolysis. Compared with IP-DIP-derived PyC (IPT8D3), the PyC_CNT sample showed an enhanced electrical conductivity, with a resistivity of 0.13 ± 0.01 Ω cm (12% reduction) (Figure 10(a)), with the enhancement due to the following reasons. First, the MWCNT in the nanocomposite photoresist can act as an MW absorber for better heating efficiency at a lower temperature under the MW irradiation [51]. Moreover, as confirmed by the Raman spectroscopy, incorporating MWCNTs leads to a more ordered carbon atomic structure after pyrolysis. While the polymer matrix undergoes pyrolysis and produces PyC at 800 °C, MWCNTs are relatively stable due to good thermal stability and do not decompose during the process. As a result, the PyC in the product may facilitate more conduction paths between the MWCNTs [52], thereby improving the electrical conductivity of the PyC_CNT.

Figure 10(b) reveals the voltammograms of IPT8D3 and PyC_CNT fabricated under the same conditions through the SMWP. Table 5 summarizes the cathodic and anodic peak currents, peak potentials and the ΔE_p. Higher peak currents (i_{pa} and i_{pc}) and lower ΔE_p is observed for the PyC_CNT electrode. This shows an improved electron transfer due to the enhanced conductivity of the PyC_CNT. The Nyquist plot from the EIS analysis and the fitting results using the Randles equivalent circuit model are presented in Figure 10(c). From the result, PyC_CNT showed a smaller semicircle with a lower R_{ct} of 164.7 ± 14.9 Ω (~20% reduction) compared to IPT8D3. This result indicated an enhanced electron transfer kinetics for the electrochemical cell using the PyC_CNT electrode.

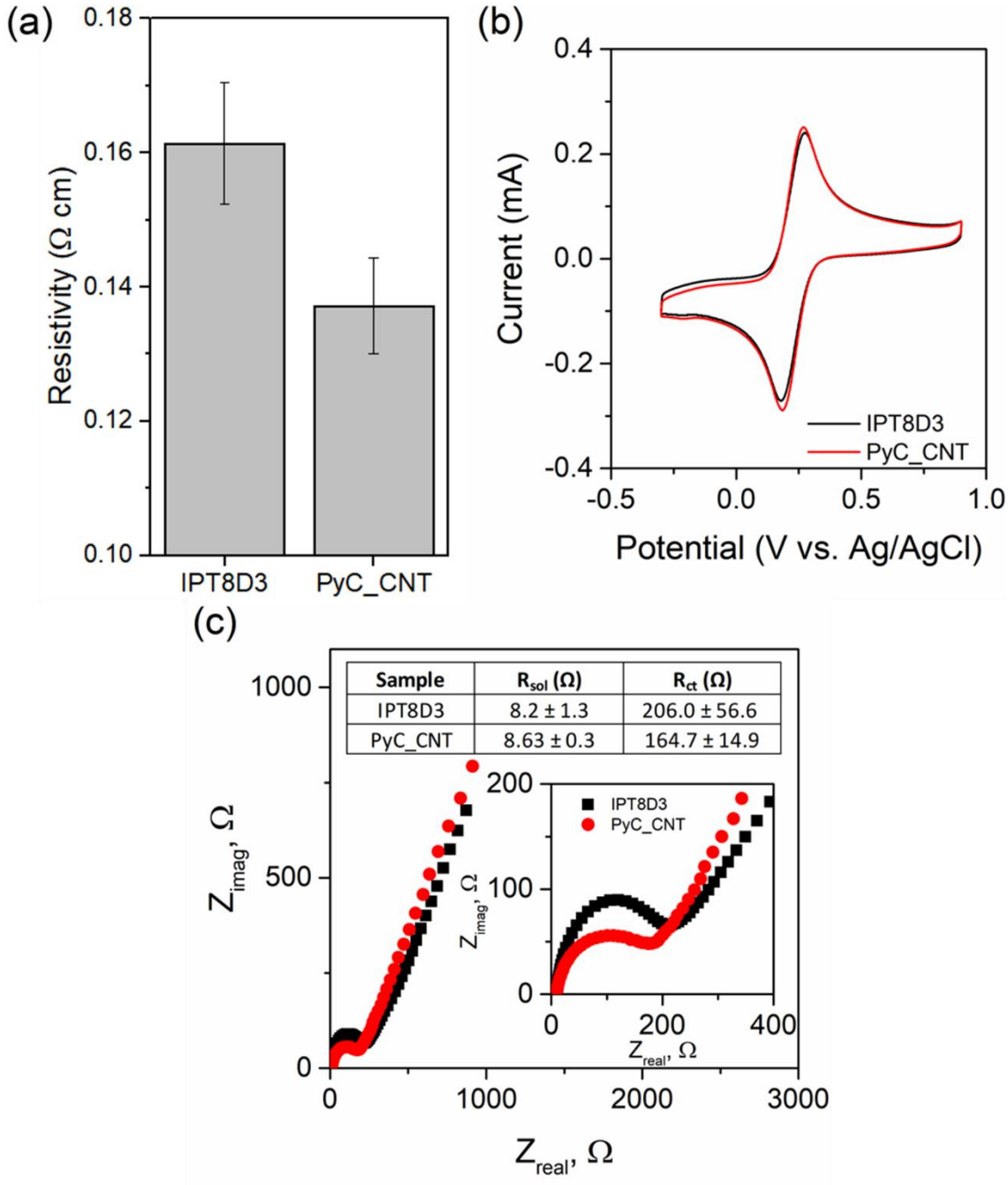

672

673 Figure 10 (a) Resistivity and (b) voltammograms of PyC-based film electrodes produced
674 through the SMWP using different photoresists at the same pyrolysis condition. (c)
675 Impedance spectra of IP-DIP-derived (IPT8D3) and SCNT-PR1-derived PyC
676 (PyC_CNT) electrodes fabricated through the SMWP

677

678 Table 5 Summary of cathodic/anodic peak currents of different photoresist-derived PyC-
679 based film electrodes fabricated through the SMWP.

PyC Sample	E_{pa} (V)	i_{pa} (mA)	E_{pc} (V)	i_{pc} (mA)	ΔE_p (mV)
IPT8D3	0.182	-0.271	0.271	0.271	89
PyC_CNT	0.186	-0.287	0.266	0.287	80

4 Conclusions

We have developed a hybrid strategy utilizing the DLW and SMWP technologies for generating predesigned 3D carbon microstructures through a detailed study of the 3D printing parameters and the SMWP conditions of an MWCNTs nanocomposite photoresist. The major findings are listed as follows:

- Thiol-functionalized MWCNT (SCNT) was successfully synthesized to improve dispersion in the acrylate-based photoresist IP-DIP.
- A printability assessment was conducted to determine optimal printing parameters, and different metamaterial microstructures with submicron resolution (833 ± 54 nm) were generated successfully using the SCNT-containing photoresist. In addition, structures containing SCNT exhibited improved stiffness compared to the unmodified IP-DIP.
- A comprehensive and comparative study of the pyrolysis condition through SMWP was conducted. It was found that SMWP can convert the polymer precursors to PyC with a more ordered carbon atomic structure due to the accelerated pyrolysis reaction under MW irradiation. As a result, better electrical properties have been achieved. For IP-DIP-derived PyC, resistivity is reduced by over 75%, from 0.69 ± 0.13 Ω cm for conventional pyrolysis to 0.16 ± 0.01 Ω cm. Enhanced electrochemical performance was also confirmed. In addition, PyC derived from the MWCNTs nanocomposite photoresist exhibited further improvement in the electrical (resistivity = 0.13 ± 0.01 Ω cm) and electrochemical performance.

- The DLW-printed metamaterials were successfully converted to 3D PyC structures while retaining their geometrical features through SMWP.

Overall, the presented effective hybrid strategy for fabricating 3D carbon-based microstructures with enhanced performance offers a very promising approach for developing miniaturized electrochemical devices.

Funding

This work was supported by a grant from the Research Committee of Hong Kong Polytechnic University under student account code RK20 and project account code G-UAMY.

References

[1] J. Feng, D. Zheng, X. Gao, W. Que, W. Shi, W. Liu, F. Wu, and X. Cao, "Three-dimensional ordered porous carbon for energy conversion and storage applications," *Frontiers in Energy Research,* vol. 8, p. 210, 2020.

[2] T. Liu, M. Li, P. Dong, Y. Zhang, and L. Guo, "Design and facile synthesis of mesoporous cobalt nitride nanosheets modified by pyrolytic carbon for the nonenzymatic glucose detection," *Sens. Actuators B Chem.,* vol. 255, pp. 1983-1994, 2018.

[3] S. Boonkaew, I. Jang, E. Noviana, W. Siangproh, O. Chailapakul, and C. S. Henry, "Electrochemical paper-based analytical device for multiplexed, point-of-care detection of cardiovascular disease biomarkers," *Sens. Actuators B Chem.,* vol. 330, p. 129336, 2021.

[4] G. Li and D. Wen, "Wearable biochemical sensors for human health monitoring: sensing materials and manufacturing technologies," *J. Mater. Chem. B,* vol. 8, no. 16, pp. 3423-3436, 2020.

[5] K. Mitsudo, Y. Kurimoto, K. Yoshioka, and S. Suga, "Miniaturization and combinatorial approach in organic electrochemistry," *Chem. Rev.*, vol. 118, no. 12, pp. 5985-5999, 2018.

[6] P. Zhang, F. Wang, M. Yu, X. Zhuang, and X. Feng, "Two-dimensional materials for miniaturized energy storage devices: from individual devices to smart integrated systems," *Chem. Soc. Rev.*, vol. 47, no. 19, pp. 7426-7451, 2018.

[7] Y. Pang, Y. Cao, Y. Chu, M. Liu, K. Snyder, D. MacKenzie, and C. Cao, "Additive manufacturing of batteries," *Adv. Funct. Mater.*, vol. 30, no. 1, p. 1906244, 2020.

[8] W. Li, Y. Zhou, I. R. Howell, Y. Gai, A. R. Naik, S. Li, K. R. Carter, and J. J. Watkins, "Direct Imprinting of Scalable, High-Performance Woodpile Electrodes for Three-Dimensional Lithium-Ion Nanobatteries," *ACS Appl Mater Interfaces,* vol. 10, no. 6, pp. 5447-5454, Feb 14 2018, doi: 10.1021/acsami.7b14649.

[9] B. AlQattan, A. K. Yetisen, and H. Butt, "Direct laser writing of nanophotonic structures on contact lenses," *ACS nano,* vol. 12, no. 6, pp. 5130-5140, 2018.

[10] A. Accardo, M. C. Blatché, R. Courson, I. Loubinoux, C. Thibault, L. Malaquin, and C. Vieu, "Multiphoton direct laser writing and 3D imaging of polymeric freestanding architectures for cell colonization," *Small,* vol. 13, no. 27, p. 1700621, 2017.

[11] L. Chen, Y. Dong, C.-Y. Tang, L. Zhong, W.-C. Law, G. C. Tsui, Y. Yang, and X. Xie, "Development of direct-laser-printable light-powered nanocomposites," *ACS Appl. Mater. Inter.*, vol. 11, no. 21, pp. 19541-19553, 2019.

[12] Z. Huang, G. C.-P. Tsui, Y. Deng, and C.-Y. Tang, "Two-photon polymerization nanolithography technology for fabrication of stimulus-responsive micro/nano-structures for biomedical applications," *Nanotechnol. Rev.*, vol. 9, no. 1, pp. 1118-1136, 2020.

[13] X. Li and H. Gao, "Smaller and stronger," *Nat. Mater.*, vol. 15, no. 4, pp. 373-374, 2016.

[14] J. U. Surjadi, L. Gao, H. Du, X. Li, X. Xiong, N. X. Fang, and Y. Lu, "Mechanical metamaterials and their engineering applications," *Advanced Engineering Materials*, vol. 21, no. 3, p. 1800864, 2019.

[15] M. S. Rill, C. Plet, M. Thiel, I. Staude, G. Von Freymann, S. Linden, and M. Wegener, "Photonic metamaterials by direct laser writing and silver chemical vapour deposition," *Nat. Mater.*, vol. 7, no. 7, pp. 543-546, 2008.

[16] T. Gissibl, S. Thiele, A. Herkommer, and H. Giessen, "Two-photon direct laser writing of ultracompact multi-lens objectives," *Nature photonics*, vol. 10, no. 8, pp. 554-560, 2016.

[17] X. W. Gu and J. R. Greer, "Ultra-strong architected Cu meso-lattices," *Extreme Mechanics Letters*, vol. 2, pp. 7-14, 2015.

[18] G. E. Lio, A. Ferraro, T. Ritacco, D. M. Aceti, A. De Luca, M. Giocondo, and R. Caputo, "Leveraging on ENZ Metamaterials to Achieve 2D and 3D Hyper-Resolution in Two- Photon Direct Laser Writing," *Adv. Mater.*, vol. 33, no. 18, p. 2008644, 2021.

[19] A. Vyatskikh, S. Delalande, A. Kudo, X. Zhang, C. M. Portela, and J. R. Greer, "Additive manufacturing of 3D nano-architected metals," *Nature communications*, vol. 9, no. 1, pp. 1-8, 2018.

[20] F. Kotz, A. S. Quick, P. Risch, T. Martin, T. Hoose, M. Thiel, D. Helmer, and B. E. Rapp, "Two- Photon Polymerization of Nanocomposites for the Fabrication of Transparent Fused Silica Glass Microstructures," *Adv. Mater.,* vol. 33, no. 9, p. 2006341, 2021.

[21] G. Konstantinou, E. Kakkava, L. Hagelüken, P. V. W. Sasikumar, J. Wang, M. G. Makowska, G. Blugan, N. Nianias, F. Marone, and H. Van Swygenhoven, "Additive micro-manufacturing of crack-free PDCs by two-photon polymerization of a single, low-shrinkage preceramic resin," *Addit. Manuf.,* vol. 35, p. 101343, 2020.

[22] K.-W. Yeung, L. Chen, C.-Y. Tang, M.-T. Choy, A. D. Akinwekomi, W.-C. Law, and G. C.-P. Tsui, "Rapid hybrid microwave cladding of SiO2/TiO2 sol–gel derived composite coatings," *Journal of Sol-Gel Science and Technology,* vol. 98, no. 1, pp. 35-44, 2021.

[23] M.-T. Choy, K.-W. Yeung, L. Chen, C.-Y. Tang, G. C.-P. Tsui, and W.-C. Law, "In situ synthesis of osteoconductive biphasic ceramic coatings on Ti6Al4V substrate by laser-microwave hybridization," *Surface and Coatings Technology,* vol. 330, pp. 92-101, 2017.

[24] A. D. Akinwekomi, K.-W. Yeung, C.-Y. Tang, W.-C. Law, and G. C.-P. Tsui, "Finite element simulation of hybrid microwave sintering based on power approach," *The International Journal of Advanced Manufacturing Technology,* vol. 110, no. 9, pp. 2503-2515, 2020.

[25] K.-W. Yeung, C.-Y. Tang, R. Hu, C.-H. Lam, W.-C. Law, G. C.-P. Tsui, X. Zhao, and J. K.-H. Chung, "Fabrication of ceramic bioscaffolds from fly ash cenosphere by susceptor-assisted microwave sintering," *Journal of the European Ceramic Society,* vol. 42, no. 10, pp. 4410-4419, 2022.

[26] M. Oghbaei and O. Mirzaee, "Microwave versus conventional sintering: A review of fundamentals, advantages and applications," (in English), *J Alloy Compd,* vol. 494, no. 1-2, pp. 175-189, Apr 2 2010, doi: 10.1016/j.jallcom.2010.01.068.

[27] P. H. M. Putra, S. Rozali, M. F. A. Patah, and A. Idris, "A review of microwave pyrolysis as a sustainable plastic waste management technique," *Journal of Environmental Management,* vol. 303, p. 114240, 2022.

[28] T. Garnault, D. Bouvard, J.-M. Chaix, S. Marinel, and C. Harnois, "Is direct microwave heating well suited for sintering ceramics?," *Ceramics International,* vol. 47, no. 12, pp. 16716-16729, 2021.

[29] J. Mao, Y. Wang, J. Zhu, J. Yu, and Z. Hu, "Thiol functionalized carbon nanotubes: Synthesis by sulfur chemistry and their multi-purpose applications," *Applied Surface Science,* vol. 447, pp. 235-243, 2018.

[30] K.-W. Yeung, Y. Dong, L. Chen, C.-Y. Tang, W.-C. Law, G. C.-P. Tsui, and D. S. Engstrøm, "Printability of photo-sensitive nanocomposites using two-photon polymerization," *Nanotechnol. Rev.*, vol. 9, no. 1, pp. 418-426, 2020.

[31] M. Chao, Y. Li, G. Wu, Z. Zhou, and L. Yan, "Functionalized multiwalled carbon nanotube-reinforced polyimide composite films with enhanced mechanical and thermal properties," *International Journal of Polymer Science,* vol. 2019, 2019.

[32] Y. Bougdid and Z. Sekkat, "Voxels optimization in 3D laser nanoprinting," *Scientific Reports,* vol. 10, no. 1, pp. 1-8, 2020.

[33] A. K. O'Brien, N. B. Cramer, and C. N. Bowman, "Oxygen inhibition in thiol–acrylate photopolymerizations," *Journal of Polymer Science Part A: Polymer Chemistry,* vol. 44, no. 6, pp. 2007-2014, 2006.

[34] C. E. Hoyle and C. N. Bowman, "Thiol–ene click chemistry," *Angew. Chem., Int. Ed. Engl.*, vol. 49, no. 9, pp. 1540-1573, 2010.

[35] L. Jiang, W. Xiong, Y. Zhou, Y. Liu, X. Huang, D. Li, T. Baldacchini, L. Jiang, and Y. Lu, "Performance comparison of acrylic and thiol-acrylic resins in two-photon polymerization," *Optics express,* vol. 24, no. 12, pp. 13687-13701, 2016.

[36] F. Jiang and D. Drummer, "Curing kinetic analysis of acrylate photopolymer for additive manufacturing by photo-DSC," *Polymers*, vol. 12, no. 5, p. 1080, 2020.

[37] P. Esfandiari, S. C. Ligon, J. J. Lagref, R. Frantz, Z. Cherkaoui, and R. Liska, "Efficient stabilization of thiol- ene formulations in radical photopolymerization," *Journal of Polymer Science Part A: Polymer Chemistry,* vol. 51, no. 20, pp. 4261-4266, 2013.

[38] W. Xiong, Y. Liu, L. J. Jiang, Y. S. Zhou, D. W. Li, L. Jiang, J. F. Silvain, and Y. F. Lu, "Laser- directed assembly of aligned carbon nanotubes in three dimensions for multifunctional device fabrication," *Adv. Mater.*, vol. 28, no. 10, pp. 2002-2009, 2016.

[39] S. Ushiba, S. Shoji, K. Masui, J. Kono, and S. Kawata, "Direct laser writing of 3D architectures of aligned carbon nanotubes," *Adv Mater,* vol. 26, no. 32, pp. 5653-7, Aug 27 2014, doi: 10.1002/adma.201400783.

[40] H. Hou, J. J. Ge, J. Zeng, Q. Li, D. H. Reneker, A. Greiner, and S. Z. Cheng, "Electrospun polyacrylonitrile nanofibers containing a high concentration of well-aligned multiwall carbon nanotubes," *Chem. Mater.*, vol. 17, no. 5, pp. 967-973, 2005.

[41] J. Song, Y. Li, D. Ke, D. Wang, and X.-E. Zhang, "In situ graphene-modified carbon microelectrode array biosensor for biofilm impedance analysis," *Electrochim. Acta,* vol. 403, p. 139570, 2022.

[42] B. Rezaei, J. Y. Pan, C. Gundlach, and S. S. Keller, "Highly structured 3D pyrolytic carbon electrodes derived from additive manufacturing technology," *Materials & Design,* vol. 193, p. 108834, 2020.

[43] K. Jurkiewicz, M. Pawlyta, D. Zygadło, D. Chrobak, S. Duber, R. Wrzalik, A. Ratuszna, and A. Burian, "Evolution of glassy carbon under heat treatment: correlation structure–mechanical properties," *J. Mater. Sci.,* vol. 53, no. 5, pp. 3509-3523, 2018.

[44] A. C. Ferrari and J. Robertson, "Interpretation of Raman spectra of disordered and amorphous carbon," *Phys. Rev. B,* vol. 61, no. 20, p. 14095, 2000.

[45] B. Pramanick, M. Vazquez-Pinon, A. Torres-Castro, S. O. Martinez-Chapaa, and M. Madou, "Effect of pyrolysis process parameters on electrical, physical, chemical and electro-chemical properties of SU-8-derived carbon structures fabricated using the C-MEMS process," *Materials Today: Proceedings,* vol. 5, no. 3, pp. 9669-9682, 2018.

[46] S. C. Moldoveanu, *Analytical pyrolysis of synthetic organic polymers*. Elsevier, 2005.

[47] P. Harris, "Fullerene-related structure of commercial glassy carbons," *Philosophical Magazine,* vol. 84, no. 29, pp. 3159-3167, 2004.

[48] A. Mardegan, R. Kamath, S. Sharma, P. Scopece, P. Ugo, and M. Madou, "Optimization of carbon electrodes derived from epoxy-based photoresist," *Journal of The Electrochemical Society,* vol. 160, no. 8, p. B132, 2013.

[49] I. Mantis, S. Hemanth, C. Caviglia, A. Heiskanen, and S. S. Keller, "Suspended highly 3D interdigitated carbon microelectrodes," *Carbon,* vol. 179, pp. 579-589, 2021.

[50] H. H. Hernández, A. M. R. Reynoso, J. C. T. González, C. O. G. Morán, J. G. M. Hernández, A. M. Ruiz, J. M. Hernández, and R. O. Cruz, "Electrochemical impedance spectroscopy (EIS): A review study of basic aspects of the corrosion mechanism applied to steels," *Electrochemical Impedance Spectroscopy,* pp. 137-144, 2020.

[51] B. Galindo, A. Benedito, F. Ramos, and E. Gimenez, "Microwave heating of polymers: Influence of carbon nanotubes dispersion on the microwave susceptor effectiveness," *Polymer Engineering & Science,* vol. 56, no. 12, pp. 1321-1329, 2016.

[52] Y. Jia, J. Yang, K. Wang, M. A. R. Chowdhury, B. Chen, Y. Su, B. C. Nickerson, and C. Xu, "Aligned carbon nanotube/carbon (CNT/C) composites with exceptionally high electrical conductivity at elevated temperature to 400 C," *Materials Research Express,* vol. 6, no. 11, p. 116302, 2019.

Fabrication of predesigned 3D carbon based microstructures via two-photon vat photopolymerization and susceptor-assisted microwave post-processing

Ka-Wai Yeung[a], Zhenjia Huang[a], Chi-Yeung Mang[a], Chak-Yin Tang[a]*, Wing-Cheung Law[a], Gary Chi-Pong Tsui[a], Xin Zhao[b]

[a]Department of Industrial and Systems Engineering, The Hong Kong Polytechnic University, Hong Kong, China

[b]Department of Applied Biology and Chemical Technology, The Hong Kong Polytechnic University, Hong Kong, China

*Corresponding author

Email address: cy.tang@polyu.edu.hk, Phone: +852 2766 6608, Fax: +852 2362 5267

Postal address: Department of Industrial and Systems Engineering, The Hong Kong Polytechnic University, Hung Hom, Kowloon, Hong Kong, China.

Declaration of interests

☒ The authors declare that they have no known competing financial interests or personal relationships that could have appeared to influence the work reported in this paper.

☐ The authors declare the following financial interests/personal relationships which may be considered as potential competing interests: